Progress Towards a Capacitively Mediated CNOT Between Two Charge Qubits in Si/SiGe

E. R. MacQuarrie,[1] Samuel F. Neyens,[1] J. P. Dodson,[1] J. Corrigan,[1] Brandur Thorgrimsson,[1] Nathan Holman,[1] M. Palma,[1] L. F. Edge,[2] Mark Friesen,[1] S. N. Coppersmith,[1,3] and M. A. Eriksson[1,*]

[1] *University of Wisconsin, Madison, WI 53706, USA*

[2] *HRL Laboratories, LLC, 3011 Malibu Canyon Road, Malibu, CA 90265, USA*

[3] *University of New South Wales, Sydney, Australia*

(Dated: August 3, 2020)

Abstract

Fast operations, an easily tunable Hamiltonian, and a straightforward two-qubit interaction make charge qubits a useful tool for benchmarking device performance and exploring two-qubit dynamics. Here, we tune a linear chain of four Si/SiGe quantum dots to host two double dot charge qubits. Using the capacitance between the double dots to mediate a strong two-qubit interaction, we simultaneously drive coherent transitions to generate correlations between the qubits. We then sequentially pulse the qubits to drive one qubit conditionally on the state of the other. We find that a conditional π-rotation can be driven in just 74 ps with a modest fidelity demonstrating the possibility of two-qubit operations with a 13.5 GHz clockspeed.

INTRODUCTION

With charge, valley, and spin degrees of freedom, quantum dots in silicon are promising hosts of many different types of qubits. Using the electronic spin state as the logical basis has enabled high fidelity single-qubit operations [1] and demonstrations of two-qubit gates [2–9]. To date, two-qubit gates in Si quantum dots have been mediated by a spin-spin exchange interaction or by coupling via a superconducting resonator [10].

Alternatively, a capacitive interaction can be used to coherently couple neighboring double dot qubits using the electronic charge degree of freedom. Capacitive coupling has been used to perform fast two-qubit operations in charge qubits [11] and singlet-triplet qubits [12, 13] in GaAs quantum dot devices.

In Si-based quantum dot devices, a strong [14] and tunable [15] capacitive interaction between double dots has been demonstrated and used to perform qubit control conditionally on the state of a classical two level system [16]. The strength of this interaction makes it a promising candidate for coupling qubits that have a tunable charge dipole moment such as the quantum dot hybrid qubit (QDHQ) [17–19]. Fast, multi-qubit control presents a number of challenges, however, such as pulse synchronization across a device. Here, we use capacitively-coupled charge qubits to explore these challenges by measuring correlated oscillations between two simultaneously-driven qubits, by using those dynamics to synchronize our multi-qubit control channels, and by using this interaction to drive a fast (74 ps) conditional π-rotation.

RESULTS

Device Details

To perform capacitively-coupled two-qubit measurements, we fabricate a linear chain of four quantum dots using an overlapping-aluminum gate architecture (Fig. 1a) [14, 15, 20, 21]. The fabrication details for this device have been reported in Ref. [15]. Measurements are performed in an Oxford Triton 400 dilution refrigerator with a ~ 15 mK mixing chamber temperature. We tune the device to host two tunnel-coupled double dots, each nominally residing in the (1,0)-(0,1) charge configuration (Fig. 1b). In all measurements reported here, the double dot electron temperature was $T_0^{\mathrm{elec}} = 228$ mK and the charge reservoir temperature was $T_0^{\mathrm{res}} = 321$ mK [22].

Two additional quantum dots are formed on the bottom half of the device to enable charge sensor readout of the qubit states. The current through the left charge sensor feeds into a room temperature current preamplifier and the resulting voltage is measured with a lock-in amplifier. The right charge sensor current is amplified at the mixing chamber of our dilution unit using a home-built two-stage cryogenic amplifier [23]. It is then amplified again at room temperature, and the resulting voltage is measured with a lock-in amplifier. While the right charge sensor only responds to the right double dot (RDD), during qubit operations the left charge sensor measures both the RDD and the left double dot (LDD). Both charge sensors are used in the measurements that follow. As detailed in Supplementary Note 2, appropriate normalization measurements allow us to subtract the calibrated RDD signal from the left charge sensor data, enabling independent measurement of the two qubits [24].

Qubit Initialization, Control, and Latched Readout

In our device, each double dot has an outer dot that neighbors a charge reservoir and an inner dot that is isolated from any reservoir. During qubit operations, we initialize each charge qubit at a large detuning ε_{I} where one electron localizes into the qubit's outer dot ($|\psi_0\rangle = |L\rangle$ for the LDD; $|\psi_0\rangle = |R\rangle$ for the RDD). Single-qubit operations are described well by a charge qubit Hamiltonian

$$H_{1\mathrm{Q}} = \frac{\varepsilon}{2}\sigma_z + t_{\mathrm{c}}\sigma_x \tag{1}$$

where ε is the double dot detuning, t_{c} is the tunnel coupling, and σ_x, σ_z are the standard Pauli operators in the position basis $\{L, R\}$. As discussed in Supplementary Note 4, we have neglected the valley excited states that can be seen in Si/SiGe quantum dot qubits [26].

To perform quantum control, we apply a fast dc pulse to move the system to $\varepsilon = 0$. This rapid pulse non-adiabatically changes the qubit Hamiltonian to generate σ_x rotations at a rate of $2t_{\mathrm{c}}$. These rotations persist until the detuning is moved back to ε_{I}. If some fraction of the electron remains in the inner dot at the end of the coherent evolution, then there is nonzero probability that a second electron will tunnel from the reservoir into the outer dot before the qubit relaxes into $|\psi_0\rangle$. When this occurs, the qubit is projected into the (1,1) charge configuration and remains there until a co-tunneling process reinitializes the qubit

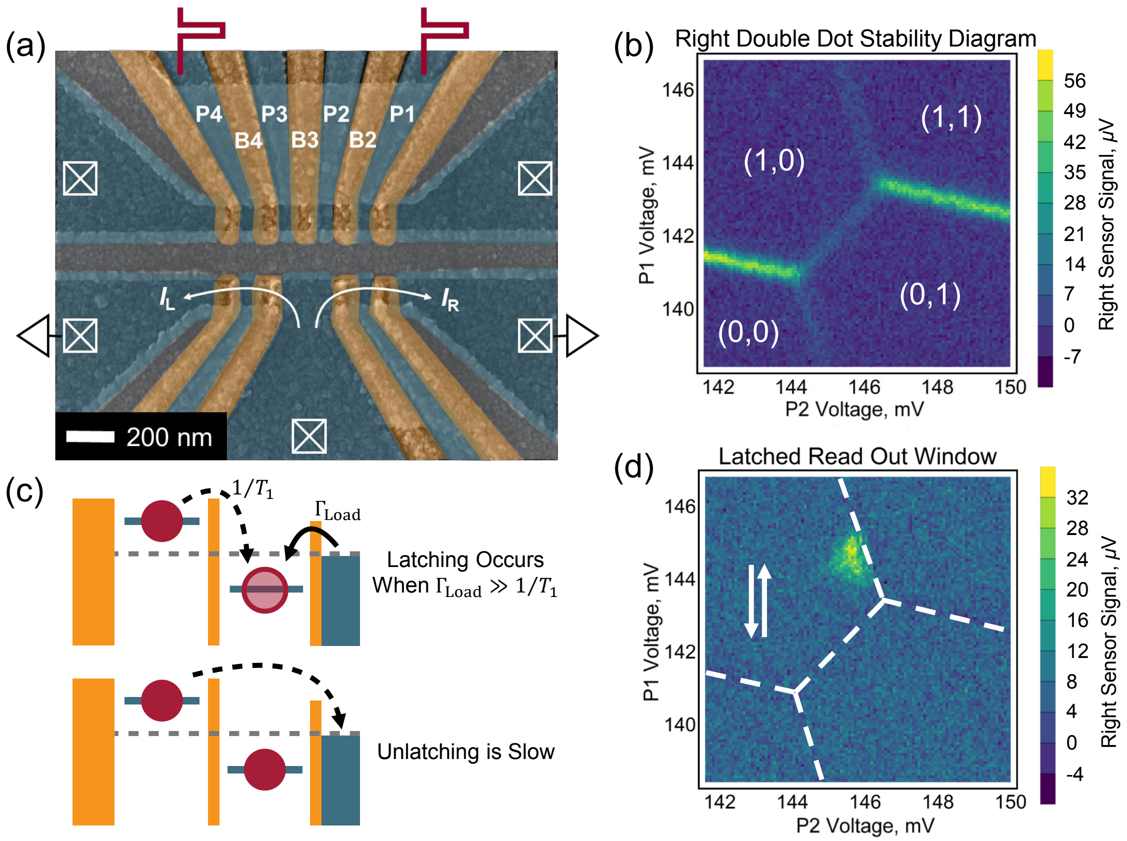

FIG. 1: Device and measurement details. (a) False-color scanning electron micrograph of a device nominally identical to the one measured here. Gates P1 and P4 are used for fast dc control as described in Supplementary Note 3 [25]. The scale bar indicates 200 nm. (b) Stability diagram of the right double dot tuned to the nominal (1,0)-(0,1) charge configuration. (c) Schematic depiction of latched state readout for the right double dot with a charge reservoir to the right and a hard-wall potential on the left. Latched readout projects the excited charge qubit state into a (1,1) charge configuration when the tunnel rate from the charge reservoir Γ_{Load} exceeds the charge qubit relaxation rate $1/T_1$. (d) Stability diagram in (b) with fast dc control pulses applied to P1. The bright triangular region indicates the latched readout window, and the white arrows illustrate the applied dc pulse.

into $|\psi_0\rangle$, providing a latched-state readout process [27, 28].

Using the metastable (1,1) charge configuration for latched-state readout provides two advantages. First, when the qubit enters the latched state, a second electron is added to the double dot system. This produces a larger shift in the charge sensor current than the mere relocation of a single electron. Secondly, this change in charge configuration persists for a much longer time because the co-tunneling process needed for reinitialization is generally much slower ($T_{\rm Latch} > 100$ ns) than charge qubit relaxation ($T_1 < 10$ ns in this device [29]). Both of these mechanisms increase the signal generated by our qubit measurements.

To maximize the probability that a driven state becomes latched, we tune the tunnel rate between the reservoir and the outer dot to be much larger than the charge relaxation rate between the two dots ($\Gamma_{\rm Load} \gg 1/T_1$). Fig. 1c provides a schematic representation of this latched measurement strategy for the RDD, and Fig. 1d shows the latched state readout window that appears when dc pulses are applied to the stability diagram in Fig. 1b. This measurement was performed by shuttering our control pulses at a fixed repetition rate, locking in to the presence and absence of control pulses, and measuring the time-averaged charge sensor response. All qubit data reported here were measured with this latched-state, time-averaged technique.

Single-Qubit Measurements

With each qubit tuned to the nominal (1,0)-(0,1) charge configuration, we use dc control pulses to perform single-qubit Ramsey measurements of the qubit inhomogeneous dephasing times T_2^*. The pulse sequence (Fig. 2a) begins with initialization at large detuning $\varepsilon_{\rm I}$. A sudden dc-shift to $\varepsilon = 0$ turns on σ_x rotations in the $\{L, R\}$ basis. After a $(n+1)\pi/2$ rotation, we apply a second dc-shift, moving to nonzero detuning and adding a σ_z component to the Hamiltonian to start phase accumulation. Returning to $\varepsilon = 0$ allows us to perform a second $(n+1)\pi/2$ rotation, projecting the accumulated phase onto the z-axis of the $\{L, R\}$ Bloch sphere. Finally, moving back to $\varepsilon_{\rm I}$ for latched state readout maps the charge qubit coherence onto the measured charge sensor current [30].

The Ramsey data for the LDD and RDD are shown in Fig. 2b,c, respectively. Both qubits display coherent behavior. By extracting the frequency of the Ramsey fringes as a function of detuning, we map the dispersion of our qubits and confirm that Eq. 1 appropriately describes each system. At large detuning ($\varepsilon/h > 30$ GHz), however, the RDD dispersion begins to deviate from the expected charge qubit behavior. This could be due to timing artifacts in our control hardware as the rotation speed surpasses the 40 ps rise time of our waveform generator. Alternatively, this could be evidence of a low-lying valley state generating additional curvature in the dispersion near $\varepsilon = 0$ [31].

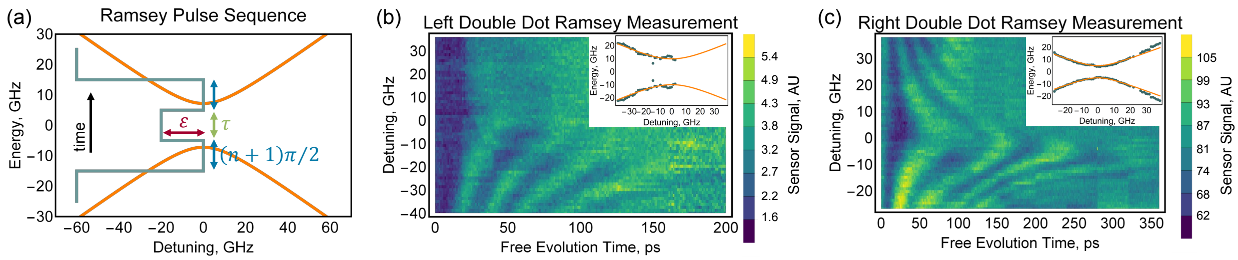

FIG. 2: Single qubit dispersions. (a) Dispersion (orange) and pulse sequence (cyan) for measuring Ramsey oscillations at a detuning ε for a free evolution time τ. (b,c) Ramsey oscillations measured in the (b) left and (c) right double dots. The extracted charge qubit dispersions with (b) $t_c^L/h = 9.9$ GHz and (c) $t_c^R/h = 5.0$ GHz are shown in the insets.

The LDD Ramsey fringes lose all visibility for free evolution at $\varepsilon > 0$. This could be due to imperfect pulse edges creating unintentional adiabaticity. Such an effect would have been more apparent in the LDD than in the RDD due to the larger tunnel coupling ($t_c^L/h = 9.9$ GHz versus $t_c^R/h = 5.0$ GHz) requiring faster rise times for true non-adiabatic control.

For large detunings, the qubit dispersion is approximately linear in ε. Assuming non-Markovian detuning noise dominates the dephasing [32], we can fit the decaying coherence to a Gaussian envelope $e^{-t^2/T_2^{*2}}$ and find that for large detunings $T_2^* = 80 \pm 20$ ps and 109 ± 6 ps for the LDD and RDD, respectively. These dephasing times can be explained by quasistatic detuning noise with standard deviations given by $\sigma_\varepsilon = h/\sqrt{2}\pi T_2^*$ where h is Planck's constant. For the LDD and RDD, we find comparable values of 12 ± 4 μeV and 8.5 ± 0.5 μeV, respectively (additional details in the SI [33]).

Correlated Oscillations

The two qubits in our device are capacitively coupled with a gate-voltage tunable coupling coefficient g [15]. In the two-qubit position basis $\{LL, LR, RL, RR\}$, the Hamiltonian describing this coupled system can be written as [11]

$$H_{2Q} = \frac{\varepsilon_L}{2}\sigma_z \otimes I + t_c^L \sigma_x \otimes I + \frac{\varepsilon_R}{2} I \otimes \sigma_z + t_c^R I \otimes \sigma_x + \frac{g}{4}(I - \sigma_z) \otimes (I - \sigma_z) \tag{2}$$

where $\varepsilon_{\rm L}$ ($\varepsilon_{\rm R}$) and $t_{\rm c}^{\rm L}$ ($t_{\rm c}^{\rm R}$) are the detuning and tunnel coupling in the LDD (RDD) and I is the identity matrix. The $\sigma_z \otimes \sigma_z$ nature of the capacitive interaction generates a detuning offset in one qubit conditionally on the state of the other (Figs. 3a,b). This capacitive interaction can be used to build state correlations between the two qubits, which we will use to synchronize one qubit's control pulses with those of the other. We note that the latched state readout described above also creates a capacitive shift upon projection into the latched state due to the introduction of an additional charge into the system. This shift is of comparable magnitude to the coherent two-qubit interaction but only appears after a qubit has been pulsed into its readout window (details in Supplementary Note 7 [34]).

In order to observe such correlations, we first tune a Hamiltonian with $t_{\rm c}^{\rm L}/h = 4.2$, $t_{\rm c}^{\rm R}/h = 3.3$, and $g/h = 15.3$ GHz. We then pulse the RDD to its anti-crossing at $\varepsilon_{\rm R} = 0$. A time Δ thereafter, we pulse the LDD to $\varepsilon_{\rm L} = g$, the location of its unshifted anti-crossing. The two qubits then simultaneously evolve according to the two-qubit Hamiltonian $H_{\rm 2Q}$. After an evolution time $\tau_{\rm L}$ ($\tau_{\rm R}$), we pulse the LDD (RDD) into its readout window for projection into the latched state. Because the latched readout state produces a capacitive shift of similar magnitude to the two-qubit interaction, the RDD (LDD) then continues evolving conditionally on the projected state of the LDD (RDD). By independently varying $\tau_{\rm L}$ and $\tau_{\rm R}$ as shown in Figs. 3c,d, we can then observe coherent two qubit dynamics along the diagonal of Figs. 3c,d where both qubits evolve at their respective anti-crossings. Away from that diagonal, we observe correlated two qubit evolution since one qubit has been conditionally projected into its latched state for some portion of the measurement. In Fig. 3d, for instance, when $\tau_{\rm L} < \tau_{\rm R} - \Delta$ the RDD continues evolving after the LDD has been pulsed to its readout window. If the LDD was projected into its latched state, the resulting capacitive shift prevents further evolution of the RDD. Otherwise, the RDD continues to oscillate with $\tau_{\rm R}$. Importantly, by using the abrupt change in charge dynamics along the diagonal of Fig. 3 as feedback, we are able to sync our fast dc pulses at the mixing chamber to within ~ 80 ps.

As shown in Fig. 3e,f, we recreate the measured two-qubit evolution by numerically solving the von Neumann equation using the Hamiltonian presented in Eq. 2. Dephasing from charge noise is included by convolving this simulation with perturbations to both $\varepsilon_{\rm L}$ and $\varepsilon_{\rm R}$ (*i.e.* $\varepsilon_i \rightarrow \varepsilon_i + \delta\varepsilon_i$). We assume these perturbations follow Gaussian distributions with standard deviations given by $\sigma_\varepsilon = 12$ and 8.5 μeV, respectively. Notably, the only

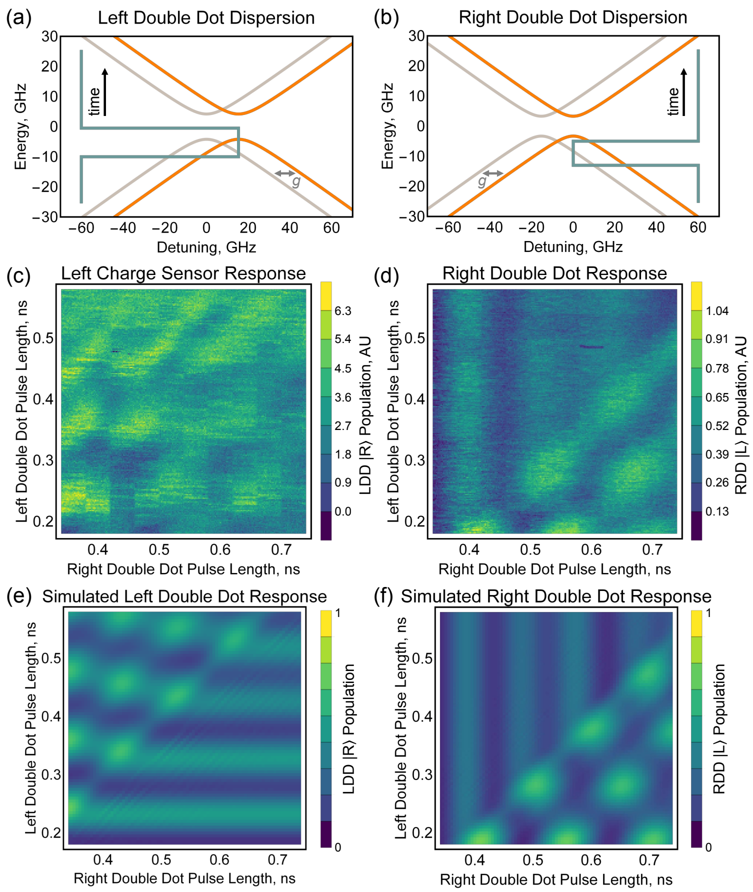

FIG. 3: Correlated qubit evolution. (a,b) Dispersions (orange) and pulse sequences (cyan) for simultaneously driving two charge qubits. Both the capacitively-shifted (light orange) and unshifted (dark orange) dispersions are shown. (c,d) Measured two-qubit response to simultaneous driving. In (c), charge sensor crosstalk has been subtracted [24], and the black pixels lie outside the range of the plotted color scale. In (d), a jump in the charge sensor has been normalized out of the data [24]. (e,f) Simulated two-qubit response to simultaneous driving. In this measurement, the right double dot pulse starts 150 ps before the left double dot pulse. We note that the time evolution in this figure occurs near each qubit's anti-crossing, so coherent oscillations persist for longer times than those in Fig. 2.

free parameter in this simulation is the fixed offset between the rising edges of the pulses, which we fix to $\Delta = 150$ ps. Additional simulation details are provided in Supplementary Note 8 [35].

Towards a Two-Qubit Gate

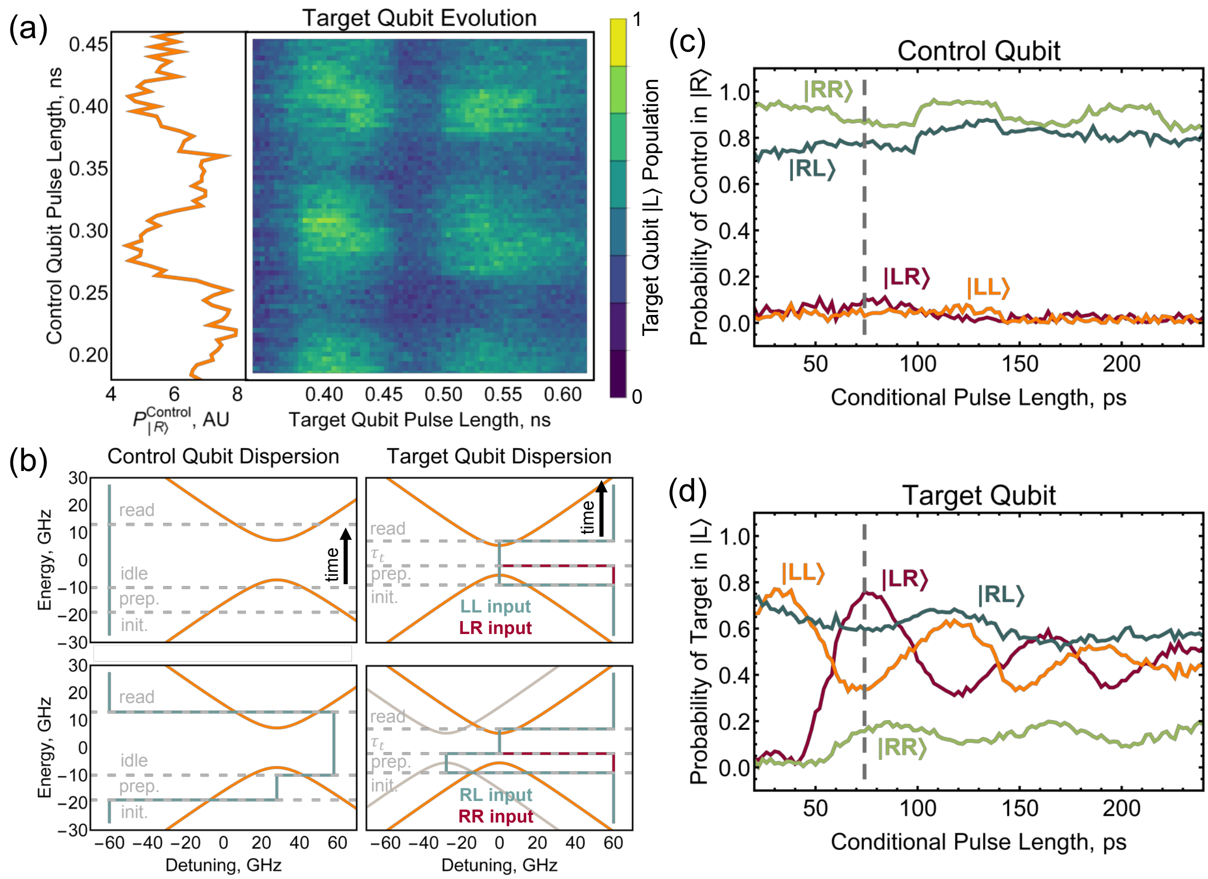

FIG. 4: Conditional qubit evolution. (a) Evolution of the target qubit conditional on the coherent driving of the control qubit. A one-dimensional slice of the control qubit evolution is plotted on the left. (b) Dispersions (orange) and pulse sequences (cyan, red) used to measure conditional rotations. The top (bottom) pair of figures was used to prepare two qubit states with the control in $|L\rangle$ ($|R\rangle$). The different control sequences used to prepare and measure the four input states are color-coded. (c,d) Evolution of the four input states in the (c) control and (d) target qubits. Charge sensor crosstalk has been subtracted from the control qubit data [24].

The capacitive interaction can also be used to drive one qubit conditionally on the state of the other as has been demonstrated experimentally in GaAs charge qubits [11] and proposed theoretically in Si/SiGe QDHQs [19]. To demonstrate conditional rotations, we designate the LDD the control qubit and the RDD the target. We shift the control qubit to $\varepsilon_{\rm L} = g$ (the location of the LDD anti-crossing for the initialized state $|LR\rangle$), allow it to evolve for some time $\tau_{\rm L}$, and then shift it to a large detuning $\varepsilon_{\rm idle}$ that lies outside the readout window. The addition of this idle step delays the conditional projection of the control qubit into its latched state, ensuring that the control qubit remains within its computational basis during target qubit operations. While the control qubit is idling, the target qubit is pulsed to $\varepsilon_{\rm R} = 0$ and is conditionally driven dependent on the state populations of the control qubit. This pulse on the target qubit constitutes our conditional driving. Both qubits are then moved into their readout windows for latched-state measurement. We note that the control qubit dephases during its idle period ($T_2^* = 80 \pm 20$ ps at $\varepsilon_{\rm idle}$), but because dephasing does not alter qubit state populations, this does not affect the target qubit evolution. The results of this measurement generate the patchwork pattern shown in Fig. 4a, which is a hallmark of conditional evolution.

Next, we characterize the fidelity of a conditional π-rotation at a tuning where $t_{\rm c}^{\rm L}/h = 7.2$, $t_{\rm c}^{\rm R}/h = 5.4$, and $g/h = 28$ GHz [34]. Our latched-state measurement technique provides the time-averaged values of $\langle \sigma_z \otimes I \rangle$ and $\langle I \otimes \sigma_z \rangle$. Without joint single shot readout or a verified, high fidelity two-qubit gate, this is not enough information to perform two-qubit tomography [36], so we restrict our analysis to input states for which both qubits are expected to evolve into single-qubit eigenstates. For these inputs, we can assume the resulting two-qubit state is separable and our readout provides the appropriate populations for construction of the truth table $M_{\rm exp}$ describing our conditional operation.

To measure $M_{\rm exp}$, we follow the pulse sequences shown in Fig. 4b to prepare each input state $\{LR, LL, RR, RL\}$. We then measure the resulting output after application of an additional driving pulse of length τ_t on our target qubit. As discussed in the SI, the charge sensor dedicated to the control qubit measures both qubits simultaneously. To account for this, we use the calibrated signal from the target qubit's charge sensor to isolate the control qubit response. We then perform a maximum likelihood estimate to ensure positive probabilities [24, 37]. Fig. 4c,d show the results of this measurement.

Selecting $\tau_t = 74$ ps maximizes the average of the logical state input fidelities (the inquisition $\mathcal{I}$ [38]) at a modest value of $\mathcal{I} = 63\%$. At this point, in the $\{LR, LL, RR, RL\}$ basis,

$$M_{exp} = \begin{pmatrix} 0.22 & 0.65 & 0.12 & 0.09 \\ 0.68 & 0.33 & 0.02 & 0.13 \\ 0.03 & 0.02 & 0.73 & 0.32 \\ 0.08 & 0.01 & 0.13 & 0.46 \end{pmatrix} \tag{3}$$

which we compare to an ideal conditional π-rotation

$$M_{\pi} = \begin{pmatrix} 0 & 1 & 0 & 0 \\ 1 & 0 & 0 & 0 \\ 0 & 0 & 1 & 0 \\ 0 & 0 & 0 & 1 \end{pmatrix}. \tag{4}$$

Notably, the input state that requires the most state preparation ($|RL\rangle$) has a significantly lower fidelity (46%) than the other input states. This suggests that state preparation errors are a dominant source of infidelity in our conditional operation, although tunnel coupling noise and state relaxation could also contribute [39].

DISCUSSION

Although the 74 ps conditional π-rotation demonstrated here is consistent with a two-qubit CNOT, the $T_2^* = 80 \pm 20$ ps dephasing time of the control qubit during its idle step limits any claim of a coherent two-qubit processor. Nevertheless, the 13.5 GHz two-qubit clockspeed highlights the benefit of using the strong capacitive interaction for inter-qubit coupling. Encoded qubits that have a tunable electric dipole moment such as the QDHQ stand to benefit from this fast gate speed without suffering from dephasing during idle periods. Compared to the charge qubits used in this work, higher fidelity single-qubit operations [18] and longer coherence times [40] for the QDHQ could also reduce state preparation errors and enable the extended pulse sequences needed for a multi-qubit processor.

In summary, we have demonstrated correlated and conditional evolution between two capacitively coupled charge qubits. After quantifying the single-qubit coherences, we simultaneously drove coherent rotations in both qubits to demonstrate correlated two-qubit evolution. We then operated in a sequential-driving mode to demonstrate a fast (74 ps) conditional π-rotation with a modest average fidelity (63%) that was likely limited by state-preparation errors. These results represent an important demonstration of the promise capacitive coupling holds for two-qubit interactions in Si/SiGe double dot qubits.

METHODS

Additional experimental details are provided in the Supplementary Information that accompanies this paper [41].

DATA AVAILABILITY

The data that support the findings of this study are available from the corresponding authors upon reasonable request.

ACKNOWLEDGMENTS

This research was sponsored in part by the Army Research Office (ARO) under Grant Number W911NF-17-1-0274 and by the Vannevar Bush Faculty Fellowship program under ONR grant number N00014-15-1-0029. We acknowledge the use of facilities supported by NSF through the UW-Madison MRSEC (DMR-1720415). The views and conclusions contained in this document are those of the authors and should not be interpreted as representing the official policies, either expressed or implied, of the Army Research Office (ARO), or the U.S. Government. The U.S. Government is authorized to reproduce and distribute reprints for Government purposes notwithstanding any copyright notation herein.

AUTHOR CONTRIBUTIONS

E.R.M., S.F.N., and M.A.E. performed the measurements and analysis. S.F.N., E.R.M., J.P.D., and N.H. designed and fabricated the device. B.T., J.C., M.P, S.F.N, and E.R.M. developed experimental protocols and hardware. L.F.E. grew the heterostructure material. E.R.M., M.A.E., M.F., and S.N.C. wrote the manuscript with feedback from all the authors. M.A.E. initiated the project and supervised the work with M.F. and S.N.C.

COMPETING INTERESTS

The authors declare no competing interests.

REFERENCES

1. Yoneda, J. *et al.* A quantum-dot spin qubit with coherence limited by charge noise and fidelity higher than 99.9%. *Nature Nanotech.* **13,** 102–106 (2018).
2. Brunner, R. *et al.* Two-Qubit Gate of Combined Single-Spin Rotation and Interdot Spin Exchange in a Double Quantum Dot. *Phys. Rev. Lett.* **107,** 146801 (2011).
3. Veldhorst, M. *et al.* A two-qubit logic gate in silicon. *Nature* **526,** 410–414 (2015).
4. Zajac, D. M. *et al.* Resonantly driven CNOT gate for electron spins. *Science* **359,** 439–442 (2018).
5. Watson, T. F. *et al.* A programmable two-qubit quantum processor in silicon. *Nature* **555,** 633–637 (2018).
6. Huang, W. *et al.* Fidelity benchmarks for two-qubit gates in silicon. *Nature* **569,** 532–536 (2019).
7. Xue, X. *et al.* Benchmarking Gate Fidelities in a Si/SiGe Two-Qubit Device. *Phys. Rev. X* **9,** 021011 (2019).
8. He, Y., Gorman, S. K., Keith, D., Kranz, L., Keizer, J. G. & Simmons, M. Y. A two-qubit gate between phosphorus donor electrons in silicon. *Nature* **571,** 371–375 (2019).
9. Sigillito, A. J., Gullans, M. J., Edge, L. F., Borselli, M. & Petta, J. R. Coherent transfer of quantum information in silicon using resonant SWAP gates. *npj Quantum Inf* **5,** 110 (2019).
10. Borjans, F., Croot, X. G., Mi, X., Gullans, M. J. & Petta, J. R. Resonant microwave-mediated interactions between distant electron spins. *Nature* **577,** 195–198 (2020).
11. Li, H.-O. *et al.* Conditional rotation of two strongly coupled semiconductor charge qubits. *Nat. Commun.* **6,** 8681 (2015).

12. Shulman, M. D., Dial, O. E., Harvey, S. P., Bluhm, H., Umansky, V. & Yacoby, A. Demonstration of Entanglement of Electrostatically Coupled Singlet-Triplet Qubits. *Science* **336,** 202–205 (2012).

13. Nichol, J. M. *et al.* High-fidelity entangling gate for double-quantum-dot spin qubits. *npj Quantum Inf* **3,** 3 (2017).

14. Zajac, D. M., Hazard, T. M., Mi, X., Nielsen, E. & Petta, J. R. Scalable Gate Architecture for a One-Dimensional Array of Semiconductor Spin Qubits. *Phys. Rev. Applied* **6,** 054013 (2016).

15. Neyens, S. F. *et al.* Measurements of Capacitive Coupling Within a Quadruple-Quantum-Dot Array. *Phys. Rev. Applied* **12,** 064049 (2019).

16. Ward, D. R. *et al.* State-conditional coherent charge qubit oscillations in a Si/SiGe quadruple quantum dot. *npj Quantum Inf* **2,** 16032 (2016).

17. Shi, Z. *et al.* Fast Hybrid Silicon Double-Quantum-Dot Qubit. *Phys. Rev. Lett.* **108,** 140503 (2012).

18. Kim, D. *et al.* High-fidelity resonant gating of a silicon-based quantum dot hybrid qubit. *npj Quantum Inf* **1,** 15004 (2015).

19. Frees, A., Mehl, S., Gamble, J. K., Friesen, M. & Coppersmith, S. N. Adiabatic two-qubit gates in capacitively coupled quantum dot hybrid qubits. *npj Quantum Inf* **5,** 73 (2019).

20. Angus, S. J., Ferguson, A. J., Dzurak, A. S. & Clark, R. G. Gate-Defined Quantum Dots in Intrinsic Silicon. *Nano Lett.* **7,** 2051–2055 (2007).

21. Borselli, M. G. *et al.* Undoped accumulation-mode Si/SiGe quantum dots. *Nanotechnology* **26,** 375202 (2015).

22. See Supplementary Note 1.

23. Tracy, L. A. *et al.* Single shot spin readout using a cryogenic high-electron-mobility transistor amplifier at sub-Kelvin temperatures. *Appl. Phys. Lett.* **108,** 063101 (2016).

24. See Supplementary Note 2.

25. See Supplementary Note 3.

26. See Supplementary Note 4.

27. Studenikin, S. A. *et al.* Enhanced charge detection of spin qubit readout via an intermediate state. *Appl. Phys. Lett.* **101,** 233101 (2012).

28. Harvey-Collard, P. *et al.* High-Fidelity Single-Shot Readout for a Spin Qubit via an Enhanced Latching Mechanism. *Phys. Rev. X* **8,** 021046 (2018).

29. See Supplementary Note 5.

30. Fujisawa, T., Hayashi, T., Cheong, H., Jeong, Y. & Hirayama, Y. Rotation and phase-shift operations for a charge qubit in a double quantum dot. *Physica E: Low Dimens. Syst. Nanostruct.* **21,** 1046 –1052 (2004).

31. Mi, X., Kohler, S. & Petta, J. R. Landau-Zener interferometry of valley-orbit states in Si/SiGe double quantum dots. *Phys. Rev. B* **98,** 161404 (2018).

32. Dial, O. E., Shulman, M. D., Harvey, S. P., Bluhm, H., Umansky, V. & Yacoby, A. Charge Noise Spectroscopy Using Coherent Exchange Oscillations in a Singlet-Triplet Qubit. *Phys. Rev. Lett.* **110,** 146804 (2013).

33. See Supplementary Note 6.

34. See Supplementary Note 7.

35. See Supplementary Note 8.

36. Vandersypen, L. M. K. & Chuang, I. L. NMR techniques for quantum control and computation. *Rev. Mod. Phys.* **76,** 1037–1069 (2005).

37. James, D. F. V., Kwiat, P. G., Munro, W. J. & White, A. G. Measurement of qubits. *Phys. Rev. A* **64,** 052312 (2001).

38. White, A. G., Gilchrist, A., Pryde, G. J., O'Brien, J. L., Bremner, M. J. & Langford, N. K. Measuring two-qubit gates. *J. Opt. Soc. Am. B* **24,** 172–183 (2007).

39. See Supplementary Note 9.

40. Thorgrimsson, B. *et al.* Extending the coherence of a quantum dot hybrid qubit. *npj Quantum Inf* **3,** 32 (2017).

41. See Supplementary Information.

Progress Towards a Capacitively Mediated CNOT Between Two Charge Qubits in Si/SiGe: Supplementary Information

E. R. MacQuarrie,[1] Samuel F. Neyens,[1] J. P. Dodson,[1] J. Corrigan,[1] Brandur Thorgrimsson,[1] Nathan Holman,[1] M. Palma,[1] L. F. Edge,[2] Mark Friesen,[1] S. N. Coppersmith,[1,3] and M. A. Eriksson[1,*]

[1] *University of Wisconsin, Madison, WI 53706, USA*

[2] *HRL Laboratories, LLC, 3011 Malibu Canyon Road, Malibu, CA 90265, USA*

[3] *University of New South Wales, Sydney, Australia*

(Dated: August 1, 2020)

SUPPLEMENTAL NOTE 1: ELECTRON TEMPERATURE

We measured the electron temperature in the double dots (electron reservoirs) of our device by sweeping through a non-tunnel-broadened polarization line (charge transition) as a function of the mixing chamber temperature T_{MC}. For each temperature measurement, linecuts were collected at a range of T_{MC} up to 350 mK and then simultaneously fit to extract an effective electron temperature. Polarization lines were fit to a standard DiCarlo function with an electron temperature of $T_e = \sqrt{T_0^2 + T_{MC}^2}$ where T_0 is the ideal electron temperature [1]. We note that this functional forms assumes an ideal charge qubit and thus ignores valley states which can lead to asymmetric lineshapes and/or modify the linewidths [2]. Charge transitions to a reservoir were fit to a Fermi-Dirac distribution [3]. The voltage-to-energy lever arms were also free parameters in these fits but were constrained to be fixed across each linecut in a given dataset.

With this method, we obtained electron temperatures of $T_0 = 228 \pm 7$ mK for the RDD and $T_0 = 321 \pm 7$ mK for the left electron reservoir. These values are exceptionally high. We believe that these temperatures could be reduced in future experiments by improving the thermal anchoring of the dc lines at the mixing chamber.

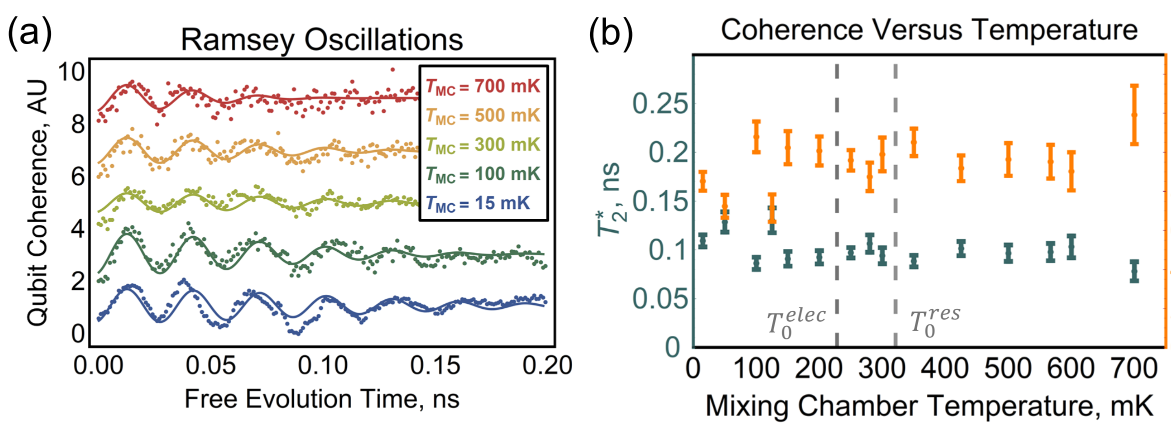

Supplementary Figure 1: Coherence versus temperature. (a) Ramsey data measured on the right double dot as a function of temperature. These linecuts were taken at $\varepsilon/h = -33$ GHz. (b) Inhomogeneous dephasing time and quasistatic charge noise extracted from the temperature-dependent Ramsey data.

To examine the prospect of operating our device at high temperatures, we measured Ramsey oscillations for the RDD as a function of the mixing chamber temperature (Supp.

Fig. 1a). Extracting T_2^* and σ_ε at each temperature (Supp. Fig. 1b), we find that coherence persists up to $T_{MC} = 700$ mK. In fact, these measurements were not limited by loss in coherence, but instead by a reduction in the visibility of our signal. At 700 mK, the lifetime of our latched state had been reduced from $T_{Latch} \sim 150$ ns to $T_{Latch} \sim 40$ ns. Although not conclusive, these results are promising for the prospect of operating qubits with a charge-like degree of freedom at higher temperatures.

SUPPLEMENTAL NOTE 2: CROSSTALK SUBTRACTION AND MAXIMUM LIKELIHOOD ESTIMATION

During our two-qubit measurements, the left charge sensor was sensitive to both the LDD and RDD qubits, whereas the right charge sensor was only sensitive to the RDD qubit dynamics. This crosstalk is demonstrated in Supp. Fig. 2. With control pulses applied to the RDD, both the right and left charge sensors detect the RDD latched-state readout window. When pulses are applied to the LDD, however, only the left charge sensor measures the LDD latched-state readout window. This crosstalk obfuscates the LDD qubit dynamics, but appropriate normalization measurements allow us to deconvolve the LDD and RDD signal from the left sensor data.

Since the right sensor only measures RDD qubit dynamics, two normalization measurements are performed for this signal. First, the right sensor is measured after the LDD and RDD qubits have been initialized into $|L\rangle$ and $|R\rangle$, respectively, providing $\mathcal{R}_{LR}$. Next, the right sensor is measured after the RDD qubit has been pulsed into the (1,1) latched state. This is done by rapidly shifting the RDD to a large negative detuning, delaying at that point until the system has relaxed into $|L\rangle$, and rapidly shifting back to the readout window for latching. This second measurement provides $\mathcal{R}_{LL}$.

The left charge sensor measures both qubits, so more normalization measurements are required to deconvolve its signal. First, the pulses described in the previous paragraph are repeated, and the left sensor current is monitored. This provides the quantities $\mathcal{L}_{LR}$ and $\mathcal{L}_{LL}$. These same measurements are then repeated again with the pulses applied to the LDD qubit instead of the RDD qubit to obtain $\mathcal{L}_{LR}$ (again) and $\mathcal{L}_{RR}$. A final normalization measurement applies pulses to both the LDD and the RDD to obtain $\mathcal{L}_{RL}$.

It is worth noting that our time-averaged measurement technique integrates signal over

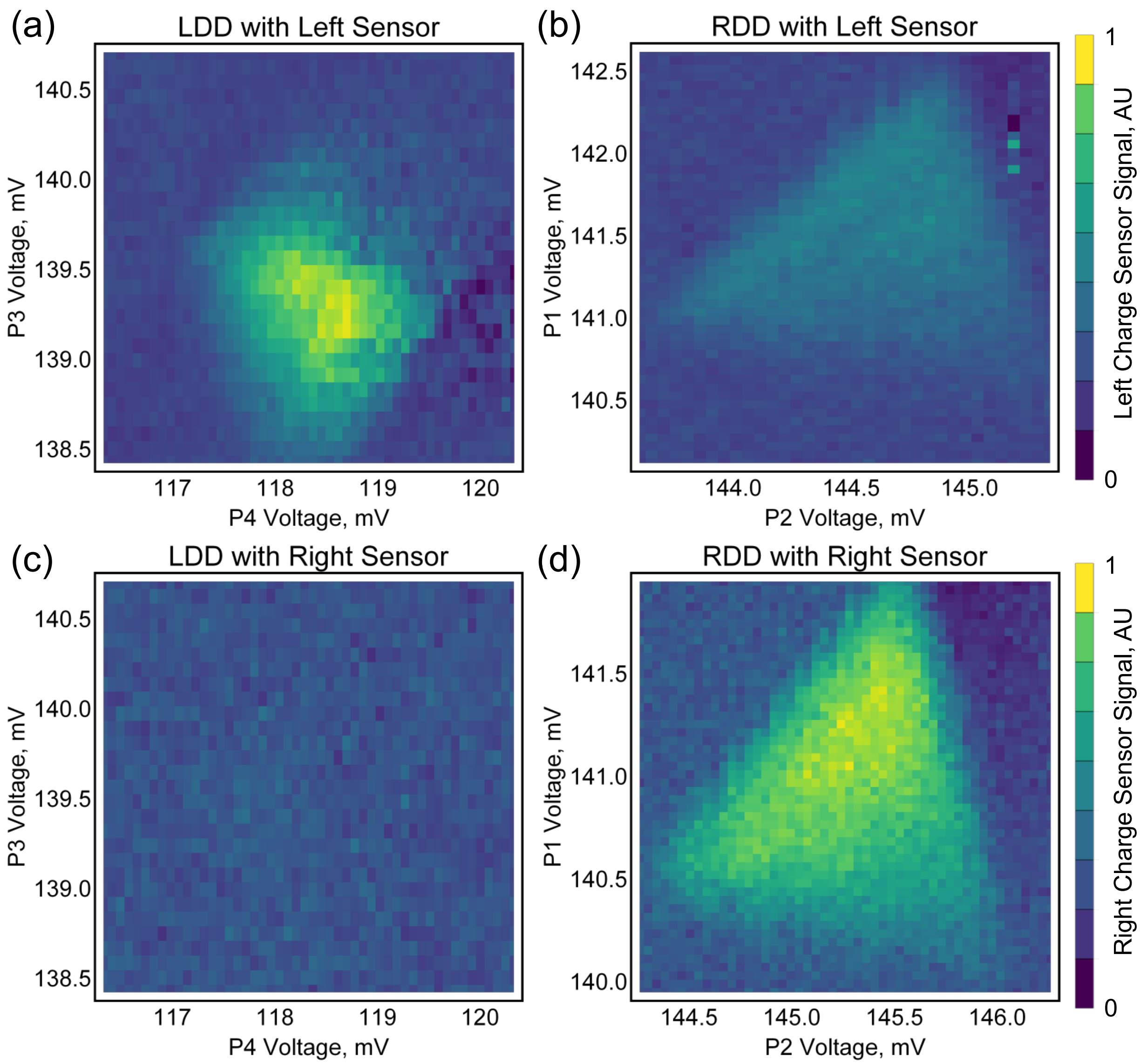

Supplementary Figure 2: Measurements of the latched-state readout windows for the (a,c) LDD and (b,d) RDD using the (a,b) left charge sensor and (c,d) right charge sensor.

the entire duty cycle of the pulse sequence. This pollutes our data with signal generated during the manipulation portion of the duty cycle. For all of our measurements, however, the manipulation time is many orders of magnitude shorter than the measurement time and any pollution is negligible. This effect is most significant for the measurements of $\mathcal{R}_{LL}$, $\mathcal{L}_{LL}$, $\mathcal{L}_{RR}$, and $\mathcal{L}_{RL}$ where the manipulation time rises to $\sim 1\%$ of the total duty cycle.

After obtaining normalization data, qubit measurements are performed to obtain the uncalibrated signal $\mathcal{L}$ and $\mathcal{R}$. Because the right charge sensor only measures the RDD qubit, we can first calibrate $\mathcal{R}$ to obtain the probability the RDD qubit has ended its evolution in state $|L\rangle$:

$$P_{|L\rangle}^{RDD} = \frac{\mathcal{R} - \mathcal{R}_{LR}}{\mathcal{R}_{LL} - \mathcal{R}_{LR}}. \tag{1}$$

The left charge sensor measures both qubits simultaneously. To account for this, we first need to determine how the two qubit signals are combined in the charge sensor response. From Supp. Fig. 2, we see that the LDD and the RDD both contribute *positively* to the left sensor signal, and comparing normalization pulses, we find $\mathcal{L}_{RR} > \mathcal{L}_{RL} > \mathcal{L}_{LL} > \mathcal{L}_{LR}$. Making the assumption of monotonic contributions to the charge sensor signal, we explain this behavior with a LDD signal whose dynamic range depends on the state of the RDD. If the RDD is in $|R\rangle$ then the LDD signal ranges from $\mathcal{L}_{RR}$ to $\mathcal{L}_{LR}$, whereas with the RDD in $|L\rangle$, the LDD contribution ranges from $\mathcal{L}_{RL}$ to $\mathcal{L}_{LL}$. The RDD contribution, however, always ranges from $(\mathcal{L}_{LL} - \mathcal{L}_{LR})$ to 0.

To apply this model to our data, we approximate the combined signal by

$$\mathcal{L} = \mathcal{L}_{LDD} + \mathcal{L}_{RDD} \tag{2}$$

where $\mathcal{L}_{RDD}$ ($\mathcal{L}_{LDD}$) is the RDD's (LDD's) contribution to the left sensor signal. The calibrated right sensor signal allows us to calculate

$$\mathcal{L}_{RDD} = P_{|1\rangle}^{RDD} \times (\mathcal{L}_{LL} - \mathcal{L}_{LR}). \tag{3}$$

Combining Eqs. 2 and 3 and calibrating with our normalization data, we can then write the probability the LDD qubit has ended its evolution in state $|R\rangle$ as

$$P_{|R\rangle}^{LDD} = \frac{\mathcal{L} - P_{|L\rangle}^{RDD} \times (\mathcal{L}_{LL} - \mathcal{L}_{LR}) - c_{min}}{c_{max} - c_{min}} \tag{4}$$

where

$$c_{min} = \mathcal{L}_{LL} P_{|L\rangle}^{RDD} + \mathcal{L}_{LR}\left(1 - P_{|L\rangle}^{RDD}\right) \tag{5}$$

and

$$c_{max} = \mathcal{L}_{RL} P_{|L\rangle}^{RDD} + \mathcal{L}_{RR}\left(1 - P_{|L\rangle}^{RDD}\right) \tag{6}$$

define the state-dependent ranges of $\mathcal{L}_{LDD}$. Notably, applying this procedure to our normalization pulses returns the expected probabilities. The data shown in Fig. 4c of the main text is replotted in Figs. 3a,b with and without the charge sensor crosstalk subtracted. For some portions of these data, this crosstalk removal procedure returns a negative probability (see Supp. Fig. 3b). To make sense of this unphysical result, we apply a maximum likelihood estimator (MLE) to our single-qubit states to enforce positivity of the reported probabilities. Because we have assumed separable states in our conditional measurements, applying this MLE at the single-qubit or the two-qubit level provides identical results.

The MLE aims to find the physically-valid density matrix ρ_p that most closely approximates our measured density matrix ρ_{exp}. Since we can only measure the diagonal elements of ρ_{exp}, we adapt the MLE protocol used in Supp. Ref. [4] to neglect coherences. We constrain ρ_p to be a non-negative, definite matrix by defining $\rho_p = \hat{T}^\dagger \hat{T} / \mathrm{Tr}[\hat{T}^\dagger \hat{T}]$ where

$$\hat{T} = \begin{pmatrix} t_1 & 0 \\ 0 & t_2 \end{pmatrix}. \tag{7}$$

We then make the assumption that for each element $\rho_{exp,i}$ imperfections in our measurements generate a Gaussian probability of measuring the physical value $\rho_{p,i}$ and the standard deviation of that distribution is approximated by $\sqrt{\rho_{p,i}}$ [4]. The probability that ρ_p could produce ρ_{exp} then becomes

$$P(\rho_{exp}) = \frac{1}{N} \prod_{i=1}^{4} \exp\left[\frac{-\left(\rho_{p,i} - \rho_{exp,i}\right)^2}{2\rho_{p,i}} \right] \tag{8}$$

where N is a normalization constant. Rather than maximizing Eq. 8, we instead maximize its logarithm, which amounts to *minimizing* the function

$$L(\rho_{exp}) = \sum_{i=1}^{4} \frac{\left(\rho_{p,i} - \rho_{exp,i}\right)^2}{2\rho_{p,i}}. \tag{9}$$

The diagonal elements of the resulting ρ_p then fill in the columns of M_{exp}, providing the truth table quoted in the main text. The results of this MLE process are shown in Supp. Fig. 3c for the control qubit and in Supp. Fig. 4 for the target qubit data.

For the data in Fig. 3 of the main text, we did not perform normalization measurements simultaneously with data acquisition. Moreover, the right charge sensor jumped during the course of the measurement. This jump created a discrete change in the charge sensor's dynamic range. To compensate for the effect of the jump, we split the data at the point of the jump and normalized each segment using the maximum and minimum values within that segment as approximations of $\mathcal{R}_{LL}$ and $\mathcal{R}_{LR}$, respectively. The effect of this procedure is demonstrated in Figs. 5a,b. We then subtracted the RDD qubit signal from the left charge sensor data using the values of $\mathcal{L}_{LL}$ and $\mathcal{L}_{RL}$ measured during our conditional measurements and approximating $\mathcal{L}_{RR}$ and $\mathcal{L}_{LR}$ with the maximum and minimum values of the raw signal.

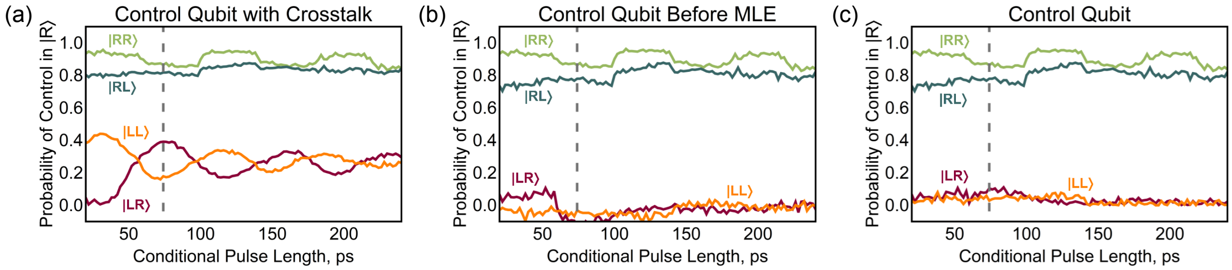

Supplementary Figure 3: The control qubit data from our conditional measurements plotted (a) with and (b) without the target qubit crosstalk included. (c) The control qubit data after the maximum likelihood estimation has been performed.

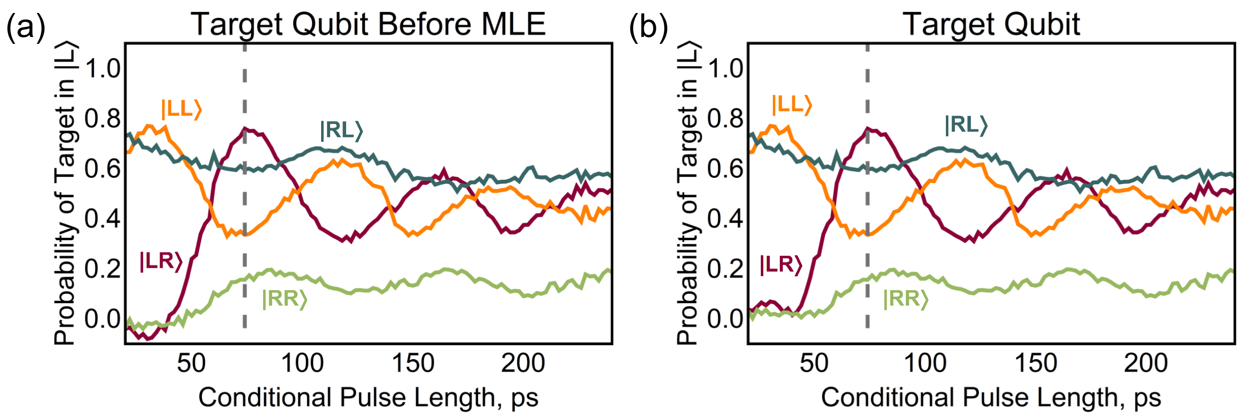

Supplementary Figure 4: The target qubit data from our conditional measurements plotted (a) before and (b) after the maximum likelihood estimation has been performed.

The effect of this subtraction is shown in Supp. Fig. 5c,d. Because we have approximated these normalization values, we plot the data with arbitrary units on the z-axis and do not apply the MLE for this measurement.

SUPPLEMENTAL NOTE 3: FAST PULSE WAVEFORM GENERATION

For each qubit, fast dc pulses were supplied by a Tektronix AWG 70001a. Internally, each waveform generator uses two interleaved 25 GS/s digital-to-analog (DAC) converters to generate a 50 GS/s waveform. We operate in a mode where, for a given AWG, each internal DAC outputs a distinct waveform. We output a positive waveform on one DAC and the negative of that same waveform plus some perturbation on the other. The internal power combiner of the AWG then sums the two waveforms, yielding just the perturbation,

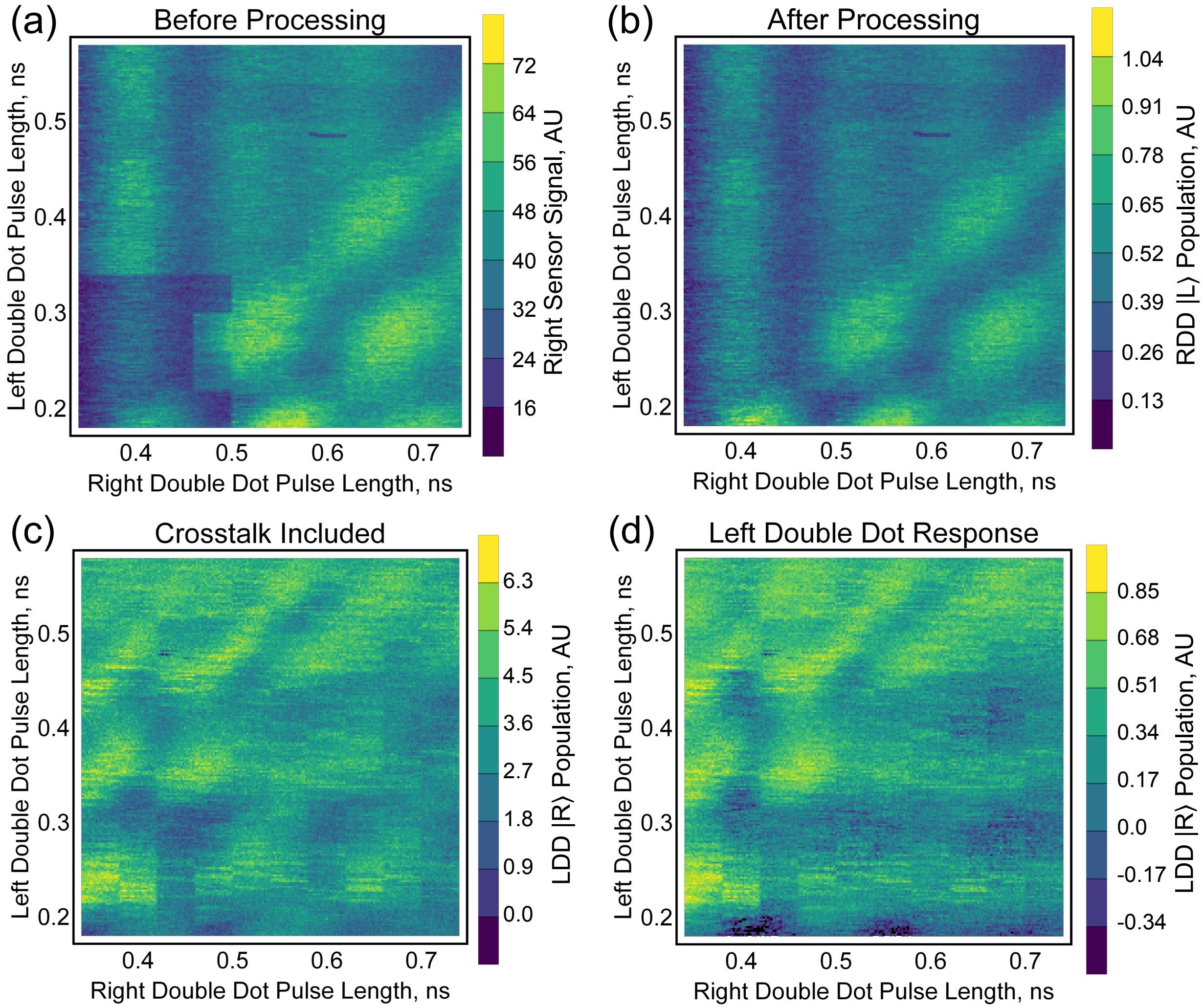

Supplementary Figure 5: Correlated oscillation data for the (a,b) RDD and (c,d) LDD. (a,b) The RDD (a) before and (b) after the data has been processed to smooth a charge sensor jump. (c,d) The LDD data (c) before and (d) after the RDD crosstalk signal has been smoothed and removed.

which we designate as our control pulse. We control the phase delay between the two DACs with 1 ps resolution, providing precise control of the generated control pulse's duration. This method is depicted schematically in Supp. Fig. 6.

For measurement sequences where multiple pulses were applied to the same qubit, this strategy of controlling the DAC phase delay only provides precise control over a single pulse edge in the sequence. Other pulses are constrained to durations that are multiples of the single DAC 40 ps sampling resolution. For the Ramsey measurements in Fig. 2 of the main text, the free evolution time τ is incremented in 1 ps steps and the $\pi/2$-pulses in the measurement were constrained to this 40 ps discretization. For our conditional measurement (Fig. 4c,d of the main text), the target qubit input state preparation pulses were constrained to this 40 ps grid. This pixelation likely contributed substantially to the state preparation errors that appear in our data.

For two-qubit measurements, both AWGs were synced at the top of the fridge using a Tektronix Sync Hub. The uncorrected time delay between the two AWGs at the bottom of the fridge was measured to be ~ 0.75 ns.

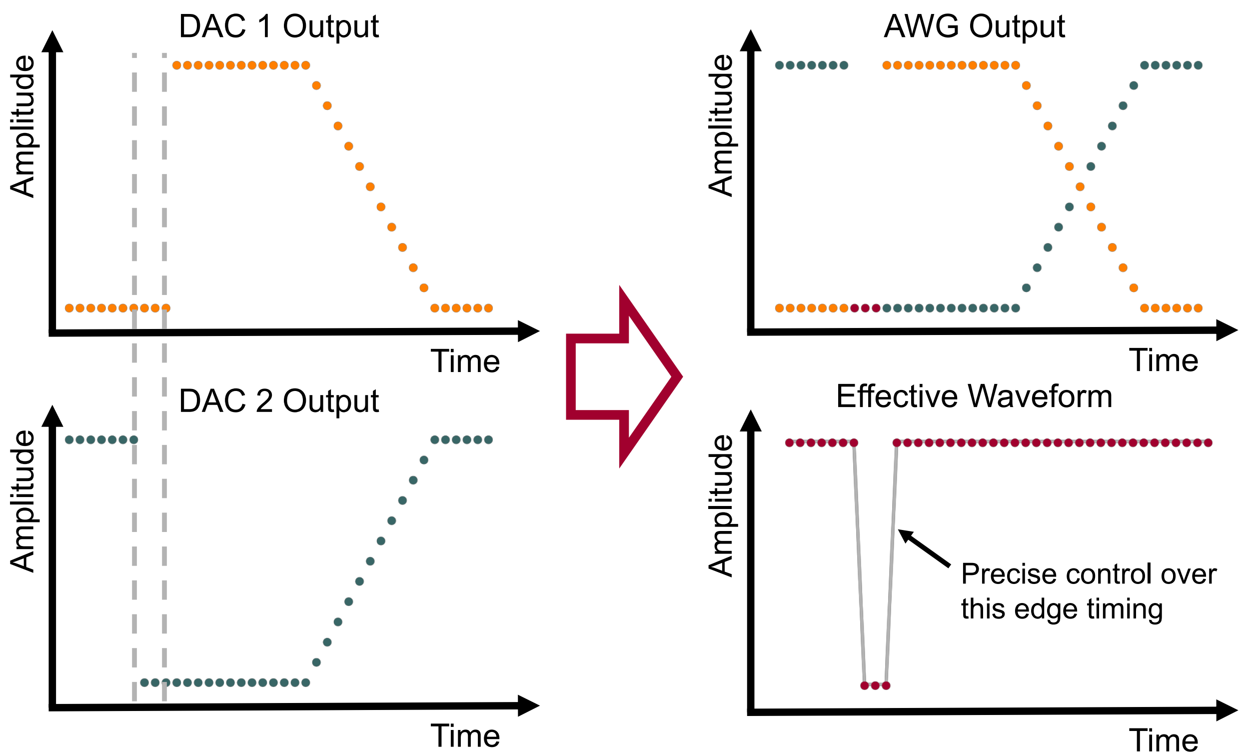

Supplementary Figure 6: Schematic representation of our strategy for generating waveforms with ∼ps timing resolution

To minimize distortions to these high speed pulses, care was taken to minimize impedance mismatches between the waveform generator and the device. Supp. Fig. 7a plots the RF transmission of the high frequency lines in our dilution refrigerator that were used in these measurements. Supp. Fig. 7b shows typical RF transmission through a nominally-identical PCB to the one on which our device was mounted. These PCB measurements were performed by wire-bonding across two on-board RF traces and measuring the throughput with a vector network analyzer. Each of these PCB measurements thus samples the transmission of two RF traces in series. Beyond the PCB, it becomes very had to know the RF response of a specific device.

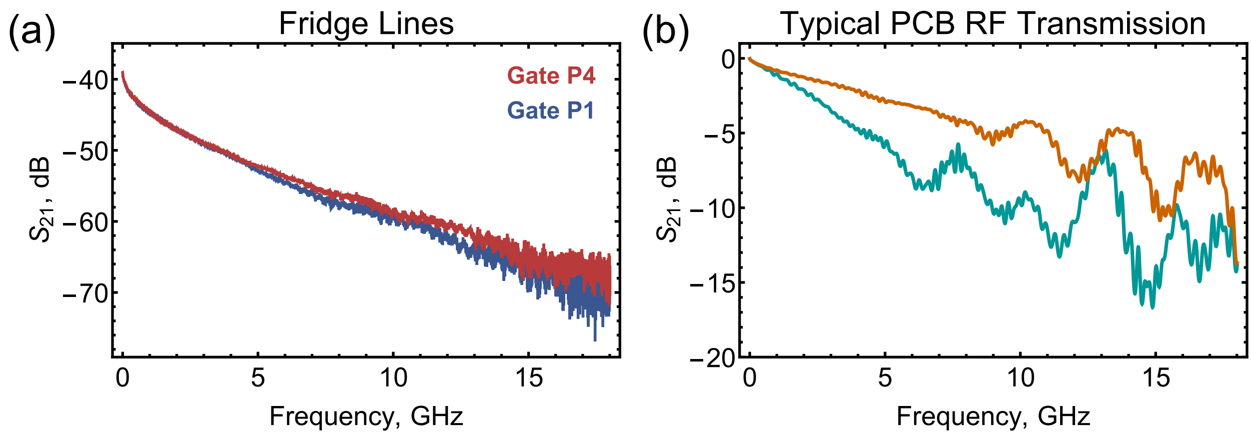

Supplementary Figure 7: RF transmission measurements. (a) RF transmission spectra for the high frequency lines of our dilution refrigerator used in these measurements. The RF lines in the fridge have −39 dB of DC attenuation added for thermalization. (b) Transmission through two pairs of RF lines of a nominally-identical PCB to the one on which our device was mounted.

SUPPLEMENTAL NOTE 4: VALLEY STATES

Throughout this manuscript, we have neglected excited valley states in our analysis of the qubit dynamics. This was done because our measurements did not resolve any sign of excited valley states and because the dispersions extracted from our Ramsey measurements (Fig. 2 of the main text) fit well to charge qubit dispersions that neglect excited valley states.

One explanation for the absence of valley states in our data would be that the valley splittings in our device are very large. Such a system could be modelled as a simple charge qubit and the dynamics would match what we have observed.

Another explanation for the apparent absence of valley splittings could be that the device's high electron temperature thermally populated a weakly-split valley manifold. Ignoring inter-valley coupling, qubit evolution would then occur independently within each valley. We do not observe beating in our Ramsey measurements, suggesting that any difference in t_c between the ground and excited valley states is less than the decoherence rate for our qubits.

Evolution within each valley state would then be indistinguishable to our measurement, and this would also have generated behavior identical to the simple charge qubit Hamiltonian we assumed in our manuscript.

Our measurements are unable to distinguish between a very large and a very small valley splitting, but similar devices we measured showed very low valley splittings (< 10 GHz) [5]. Because of this, we judge the latter case to be the more likely reality.

SUPPLEMENTAL NOTE 5: T_1 AND T_{Latch} MEASUREMENTS

Following the method described in Supp. Ref. [6], we measured the relaxation time T_1 of our two charge qubits. For both qubits, we measured $T_1 < 10$ ns (Supp. Fig. 8), which is short enough to prohibit ac driving of our charge qubits [7]. We speculate that this short relaxation time stems from increased electron-phonon scattering due to our high electron temperature.

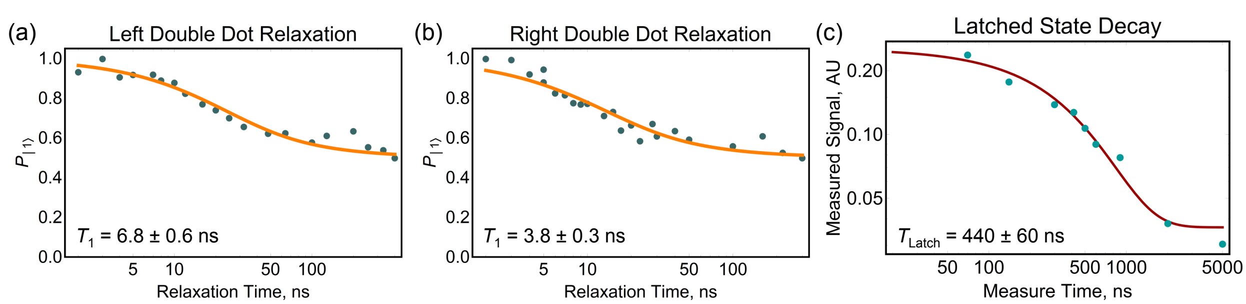

Supplementary Figure 8: Charge state relaxation. (a,b) T_1 measurements for the (a) left double dot and (b) right double dot. (c) Measurement of the latched state lifetime T_{Latch}.

A similar measurement technique enabled us to quantify the lifetime of the latched readout state. The latched state was controllably prepared and allowed to persist for a variable time τ by modifying the duty cycle of the measurement. Supp. Fig. 8c shows the resulting decay in signal, which we fit to find $T_{Latch} = 440 \pm 60$ ns for this tuning.

SUPPLEMENTAL NOTE 6: FITTING RAMSEY DATA

To extract the inhomogeneous dephasing time T_2^*, we neglect any valley or spin degrees of freedom and fit the charge qubit coherence ρ_{LR} to the function

$$\rho_{LR} = Ae^{-\tau^2/T_2^{*2}} \cos(\omega\tau + \phi) + B \tag{10}$$

where A and B are constants, τ is the free evolution time, ω is the qubit frequency at a given detuning, and ϕ is a fixed phase offset.

To extract the charge qubit dispersions shown in the insets of Fig. 2a,b of the main text, we fit linecuts of the data to Eq. 10. For the LDD data, the Ramsey fringe visibility vanishes for $\varepsilon > 0$. The background level also drifts with the free evolution time τ in these data. To correct for this, we average all linecuts with $\varepsilon/h > 8.9$ GHz where the fringe visibility has vanished and subtract this mean from the rest of the data before fitting. The $\sigma_\varepsilon = 12 \pm 4$ μeV value for the LDD quasistatic charge noise was obtained by averaging the T_2^* values returned from the fits for all $\varepsilon/h < -27.5$ GHz at which point $|\partial\omega/\partial\varepsilon| > 0.8$.

Charge qubits exhibit a reduced sensitivity to charge noise when operated near their anti-crossing. This creates the prolonged dephasing time for detunings near zero in Fig. 2 of the main text. Fitting linecuts of these data (Supp. Fig. 9), we can demonstrate this enhancement by observing a T_2^* increase from $T_2^*(\varepsilon/h = 20 \text{ GHz}) = 109 \pm 6$ ps to $T_2^*(\varepsilon/h = -5.2 \text{ GHz}) = 330 \pm 20$ ps for the RDD and $T_2^*(\varepsilon/h = 31 \text{ GHz}) = 75 \pm 15$ ps to $T_2^*(\varepsilon/h = 9.3 \text{ GHz}) > 200$ ps for the LDD.

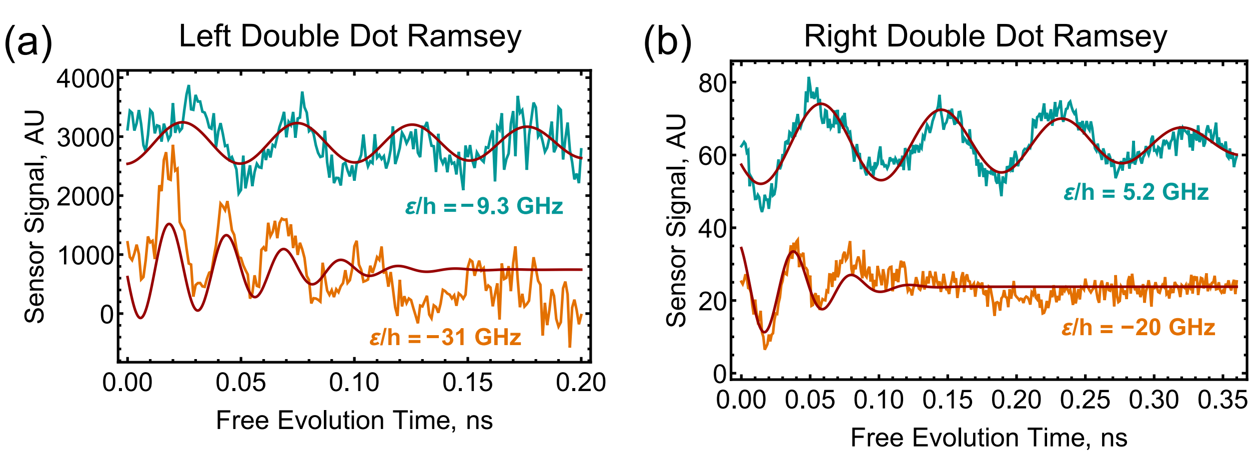

Supplementary Figure 9: Linecuts of Fig. 2 in the main text demonstrating an increase in the dephasing time for detunings near zero in the (a) left and (b) right double dot.

When fitting the Ramsey measurements performed as a function of temperature (Supp. Fig. 1 in the SI), we fix ϕ and ω at each detuning to be the same for every temperature. The data in Supp. Fig. 1b are the average results for linecuts in the detuning range $\varepsilon/h \in (-33, -29)$ GHz. The $\sigma_\varepsilon = 8.5 \pm 0.5$ μeV value of the RDD quasistatic charge noise quoted in the main text was extracted from the $T_{MC} = 15$ mK datum in this measurement.

To compare these charge noise values to those reported elsewhere, we assume the quasistatic value we measure comes from a $S_\varepsilon(f) \sim 1/f$ noise spectrum integrated from the bandwidth of our lock-in amplifier $1/\tau_M$ where $\tau_M = 50$ ms to 31 GHz for the RDD and 33 GHz for the LDD. This gives charge noise values of $S_\varepsilon^{1/2}(1\text{ Hz}) = 1.3$ $\mu\text{eV}/\sqrt{\text{Hz}}$ for the RDD and 1.8 $\mu\text{eV}/\sqrt{\text{Hz}}$ for the LDD, both of which are reasonable values for a Si/SiGe device with a 30 nm deep quantum well and 5 nm of Al_2O_3 gate oxide [8].

SUPPLEMENTAL NOTE 7: CAPACITIVE SHIFT OF LATCHED STATE

As discussed in the main text, shelving one double dot into its metastable latched state produces a capacitive shift in the other double dot. For our conditional measurements, we move the control qubit to an idle point during target qubit operations. This delays projection into the latched state until after our conditional rotation is complete, ensuring that any conditional behavior we detect results from the capacitive interaction between the two qubits.

Our measurement of correlated oscillations in Fig. 3 of the main text did not use idle points to delay projection into the latched state. This means that once we deviate from the diagonal that defines synchronized pulse tails, one qubit has been moved into its readout window and might have been projected into its latched state. However, extending the classical capacitance network model described in Supp. Ref. [9], we can show that to first order in interdot capacitances the double dot capacitive shift g is equal to the capacitive shift from the latched state g_{Latch}. For the simulation shown in Figs. 3e,f, we therefore use $g = g_{Latch} = 15.3 \times h$ GHz. This relation between g and g_{Latch} was verified via electrostatic measurements at the device tuning used for our conditional measurements (Supp. Fig. 10) and is expected to hold at the tuning used in Fig. 3 of the main text.

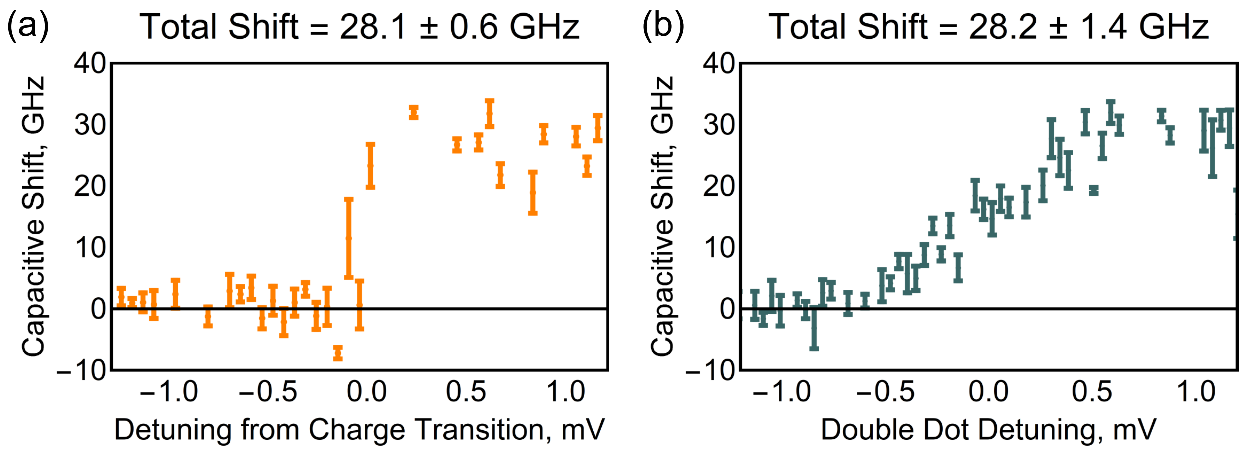

Supplementary Figure 10: Capacitive shift experienced by the right double dot due to a transition in the left double dot from (a) the (1,0) to the (1,1) charge state and (b) the (1,0) to the (0,1) charge state. Note that the abrupt transition in (a) is because the charge transition being swept is a cotunneling process with a relatively slow tunnel rate [9].

SUPPLEMENTAL NOTE 8: SIMULATIONS OF CORRELATED OSCILLATIONS

The simulation results presented in Fig. 3e,f of the main text were obtained by numerically solving the von Neumann equation

$$i\hbar \frac{\partial \rho}{\partial t} = [H_{2Q}, \rho]. \tag{11}$$

Here, $\hbar$ is the reduced Planck constant, ρ is the density matrix for the two-qubit system, and H_{2Q} is the Hamiltonian presented in Eq. 2 of the main text. This Hamiltonian is written in the $\{LL, LR, RL, RR\}$ basis and does not include either qubit's latched state. Because $g \sim g_{Latch}$ (Supplemental Note 7), the only change in H_{2Q} upon the projection of one qubit into its latched state is that the tunnel coupling for that qubit goes to zero ($t_c^i \to 0$). Latched state projection only occurs when $\varepsilon_i \gg t_c^i$, at which point the effect of t_c^i on the charge dynamics is already negligible. This means that the model described above is a good approximation of the measurement both before and after latched state projection. Because we do not have a precise measurement of Γ_{Load}, we restrict the simulation to the $\{LL, LR, RL, RR\}$ basis and assume the effects of t_c^i are negligible when $\varepsilon_i \gg t_c^i$.

Dephasing was included in the simulation by adding a perturbation to each double dot's detuning ($\varepsilon_i \to \varepsilon_i + \delta\varepsilon_i$), convolving the simulation with Gaussian distributions of $d\varepsilon_L$ and $d\varepsilon_R$, and normalizing appropriately. To verify the simulation reproduced the experimentally-measured coherence times, we simulated single qubit dephasing measurements in the large-detuning regime (Supp. Fig. 11).

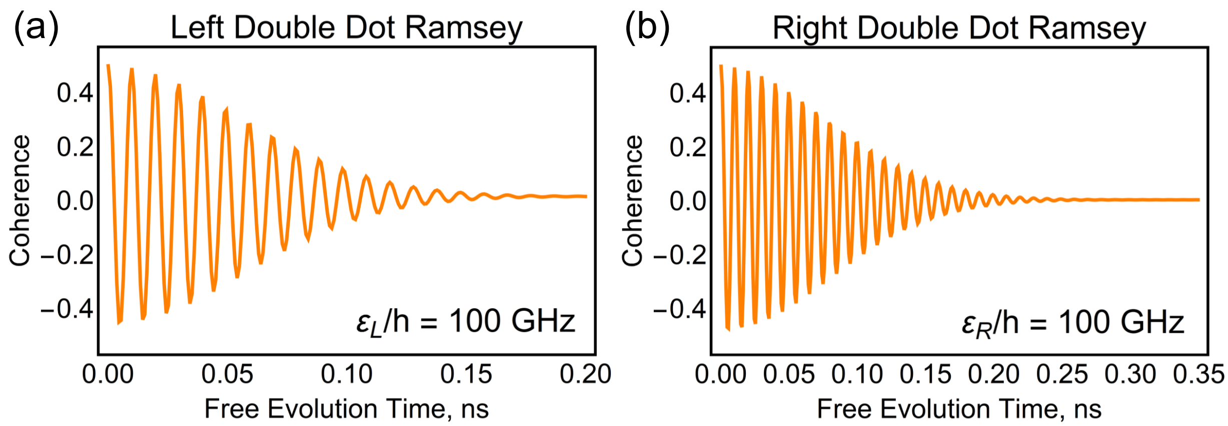

Supplementary Figure 11: Simulations of single qubit dephasing for the (a) left double dot and (b) right double dot.

SUPPLEMENTAL NOTE 9: SIMULATIONS OF CONDITIONAL OSCILLATIONS

To verify our understanding of the conditional oscillations presented above, we model these measurements using the simulations described in the previous section. For these simulations, we use the parameters quoted in the main text: $t_c^L/h = 7.2$, $t_c^R/h = 5.4$, and $g/h = 28$ GHz. We assume ideal non-adiabatic pulses for state preparation. Supp. Fig. 12 shows the results of these measurements. Because our simulations do not include tunnel coupling noise or state relaxation, they do not accurately recreate the decay envelope observed in Fig. 4d of the main text. The ideal pulses of the simulation also do not contain the initial distortion shown in Fig. 4d, placing the conditional π-rotation at 46 ps with a simulated mean fidelity of $\mathcal{I} = 81\%$.

In Supp. Fig. 13a,b, we present those same simulations but with g reduced to $g/h =$ 2.8 GHz. In this weak coupling limit, we see a dramatic reduction in the expected fidelity of the two-qubit interaction. Ignoring dephasing, relaxation, and state preparation errors altogether, the target qubit dynamics can be modeled by Rabi's formula with a Rabi frequency of $2t_c$ and a detuning of 0 for when the control qubit is in $|L\rangle$ and $-g$ for the control in $|R\rangle$ [10]. Plotting the maximum inquisition as a function of both t_c and g (Supp. Fig. 13c), we see the border between strong and weak capacitive coupling in an ideal two charge qubit

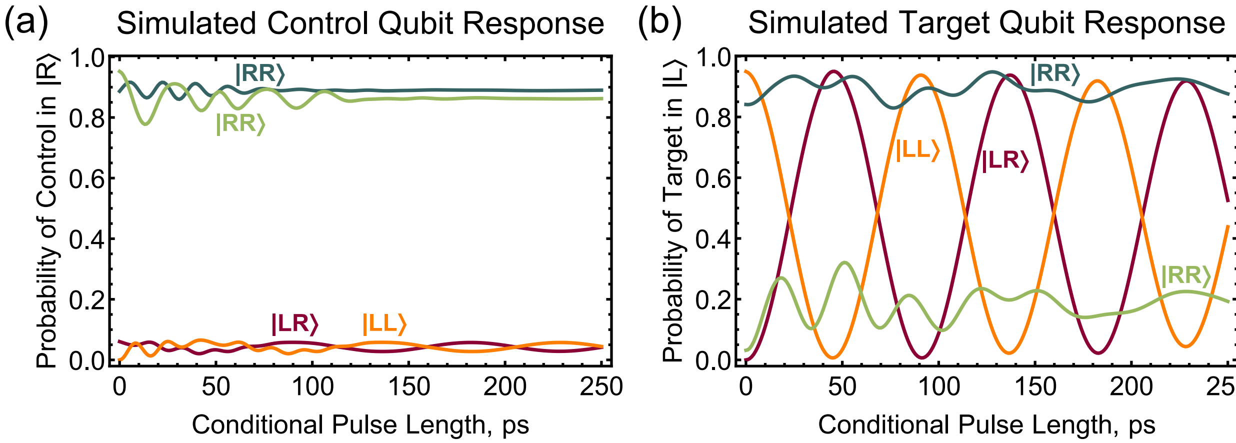

Supplementary Figure 12: Simulated response of the (a) control and (b) target qubits to the measurement sequence depicted in Fig. 4c,d of the main text. The simulation ignores tunnel coupling noise and state relaxation and thus fails to recreate the decay envelope observed in the measurement.

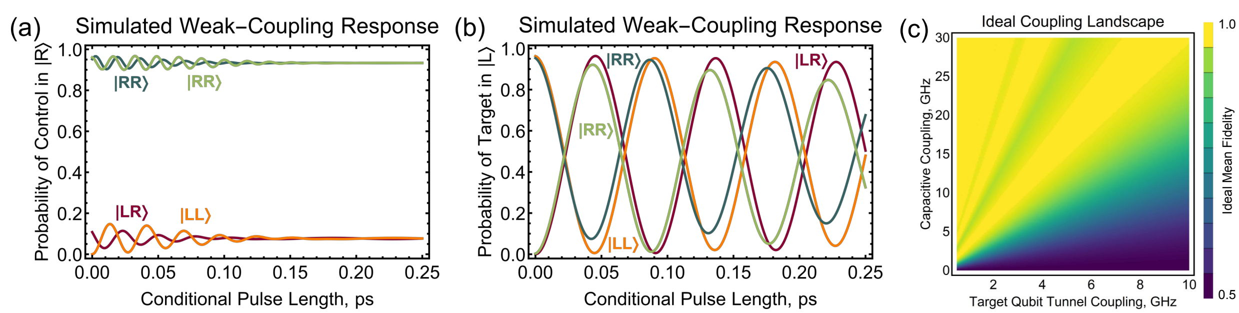

Supplementary Figure 13: Weak coupling simulations. (a,b) Simulated response of the (a) control and (b) target qubits in the case of realistic weak capacitive coupling. (c) Calculated mean fidelity for an ideal two charge qubit system.

system. For the parameters of our measurements ($t_c/h = 5.4$ GHz, $g/h = 28$ GHz), we sit comfortably in the strongly coupled region.

SUPPLEMENTARY REFERENCES

1. DiCarlo, L. *et al.* Differential Charge Sensing and Charge Delocalization in a Tunable Double Quantum Dot. *Phys. Rev. Lett.* **92,** 226801 (2004).

2. Zhao, X. & Hu, X. Coherent electron transport in silicon quantum dots. *arXiv:1803.00749* (2018).

3. Maradan, D. *et al.* GaAs Quantum Dot Thermometry Using Direct Transport and Charge Sensing. *J. Low Temp. Phys.* **175,** 784–798 (2014).

4. James, D. F. V., Kwiat, P. G., Munro, W. J. & White, A. G. Measurement of qubits. *Phys. Rev. A* **64,** 052312 (2001).

5. Dodson, J. P. & Eriksson, M. A. Private Communication. Madison, WI, USA, 2020.

6. Wang, K., Payette, C., Dovzhenko, Y., Deelman, P. W. & Petta, J. R. Charge Relaxation in a Single-Electron Si/SiGe Double Quantum Dot. *Phys. Rev. Lett.* **111,** 046801 (2013).

7. Kim, D. *et al.* Microwave-driven coherent operations of a semiconductor quantum dot charge qubit. *Nature Nanotechnol.* **10,** 243 (2015).

8. Connors, E. J., Nelson, J., Qiao, H., Edge, L. F. & Nichol, J. M. Low-frequency charge noise in Si/SiGe quantum dots. *Phys. Rev. B* **100,** 165305 (2019).

9. Neyens, S. F. *et al.* Measurements of Capacitive Coupling Within a Quadruple-Quantum-Dot Array. *Phys. Rev. Applied* **12** (2019).

10. Sakurai, J. J. *Modern Quantum Mechanics; rev. ed.* (Addison-Wesley, Reading, MA, 1994).